Tatra Mt. Math. Publ. ?? (2026), 1–36
DOI: 10.2478/tmmp-2026-0005

TATRA MOUNTAINS
Mathematical Publications

MATHEMATICAL AND NUMERICAL METHODS FOR ACCURATE AORTA SEGMENTATION FROM NON-ENHANCED CT DATA YIELDING RELIABLE IDENTIFICATION AND EVALUATION OF LARGE VESSEL VASCULITIS

Konan A. Allaly[1,2] — Jozef Urbán[2] — Karol Mikula[1]

[1]Department of Mathematics and Descriptive Geometry, Slovak University of Technology, Bratislava, SLOVAKIA

[2]TatraMed Software s.r.o., Bratislava, SLOVAKIA

ABSTRACT. Segmentation of the aorta is crucial for various medical analyses, such as the diagnosis and treatment of cardiovascular diseases. This work presents mathematical models and methods yielding a semi-automatic segmentation of the aorta from non-enhanced CT data. Our framework consists of three steps. First, using the minimal path approach, we extract a path within the aorta from two user-supplied points. Then, using 3D Lagrangian curve evolution, we move the initial path to the approximate centerline of the aorta. The centered path is used in the last step to construct the initial condition for the generalized subjective surface method (GSUBSURF). Applying the GSUBSURF method with this initial condition yields an accurate segmentation of the aorta. The segmentation results and the manual segmentations overlap, with a worst-case mean Hausdorff distance of 2.175 ± 0.605 mm for a voxel spacing of 0.977 mm. Using the aorta centerline and segmentation, we define precise regions of interest along the aorta to assess large-vessel vasculitis from patient FDG-PET/CT image data. The application shows promising results, as we demonstrated widespread inflammation throughout the aorta in a patient prior to treatment. After treatment, we observed a significant reduction in inflammation and accurately identified the aortic regions where it persisted. These findings also align with those of experienced medical doctors who have worked on the same cases.

2020 Mathematics Subject Classification: 35A18, 58J32, 65D18, 68U10.
Keywords: Segmentation, minimal path, curve evolution, large-vessel vasculitis.
This work was supported by the grant Marie Sklodowska-Curie no. 955576. The grant APVV no. 23-0186, and the grant VEGA no. 1/0249/24.

1. Introduction

Vasculitis is inflammation of blood vessels of various sizes. Early detection and treatment are crucial to prevent irreversible damage, such as loss of vision in retinal vasculitis and aortic dissection when the aorta is involved [13]. Various approaches are used to diagnose vasculitis, including biopsy and imaging. Numerous studies conducted by rheumatologists, radiologists, clinicians, and researchers [4, 13, 40, 42] have demonstrated the role of ^{18}F-fluorodeoxyglucose-positron emission tomography (FDG-PET) imaging in the classification, diagnosis and follow-up of vasculitis. Two approaches are used to interpret FDG-PET images: visual and quantitative analysis [40]. A radiologist performs the visual analysis, and the result depends on the user's experience. For quantitative analysis, regions of interest (ROIs), including the vessel wall, are manually extracted for interpretation. Due to the low resolution of PET images, and to better define ROIs, FDG-PET images are often combined with another scan in the same coordinate system, such as Computed Tomography (CT), where anatomical structures are more clearly visible. Therefore, this work focuses on the precise segmentation of the aorta from CT data to define the precise ROIs in FDG-PET image data.

The aorta is the main artery of the human body, which transports oxygen-rich blood from the heart to the rest of the body. The aorta is a tube-like structure divided into anatomical segments, including the aortic root, ascending aorta, aortic arch, descending thoracic aorta and abdominal aorta (see Fig. 1).

Due to its importance, researchers have been intensively working on segmenting the aorta from magnetic resonance imaging (MRI), computed tomography angiography (CTA), and CT images [17, 22, 24, 41, 43, 44]. Segmenting the aorta from non-enhanced CT data is challenging due to noise, weak or missing edges, low contrast, and proximity to other organs with similar intensity. Two main approaches are used to detect the aorta in non-enhanced CT data. Some algorithms use a priori models built from manually segmented training data. The other algorithms use anatomical information and the Hough Transform to detect the aorta in a given slice as a circular shape. Thresholding and region growing [1, 8] are widely used to segment medical images, giving promising results when the image contrast is high. However, they lead to over-segmentation for low-contrast or highly noisy images. Deformable models [9, 21, 38] are also used for medical image segmentation, but require good initial condition and strong edges to achieve optimal results. Recently, machine learning and deep learning algorithms have been investigated and used to segment the aorta [41, 44]. Various approaches have been proposed to segment the aorta in different image modalities. The available works proposed for non-enhanced CT data focused only on the thoracic aorta. Kurugol et al. [24] proposed an automatic aorta segmentation method using the Hough transform and level sets in non-contrast chest CT data.

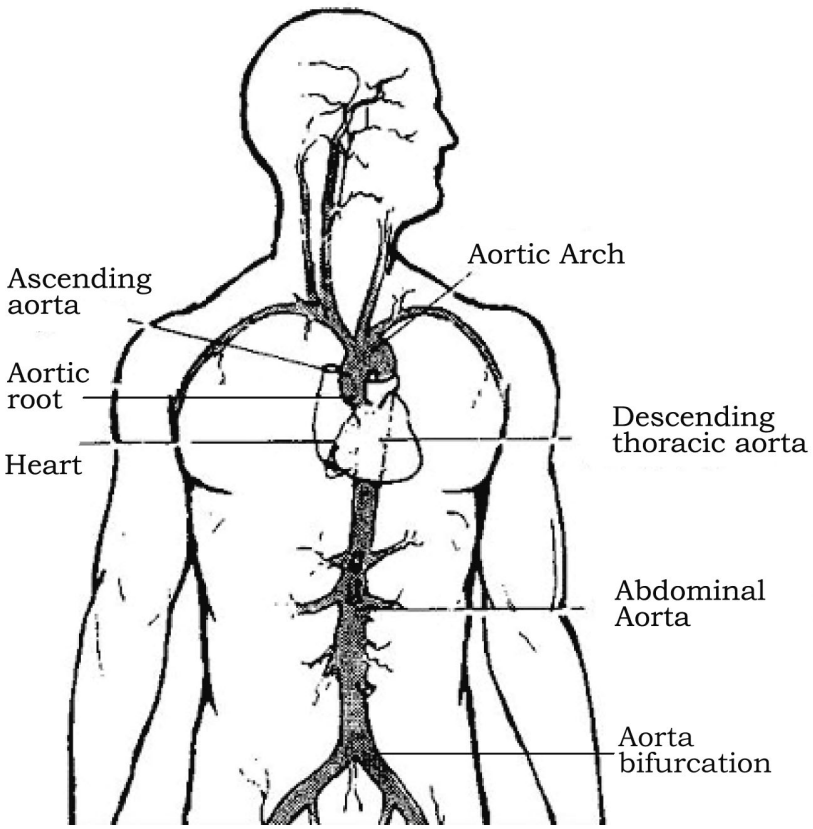

FIGURE 1. Aorta location in the body [22].

The algorithm detects the ascending and descending aorta in the heart region using the Hough transform. The centers of detected circles are used to reconstruct the aorta's initial surface. The initial surface is finally refined using 3D level--set evolution. Lower segmentation accuracy is observed around the aortic arch, attributed to limitations in ground-truth accuracy. Martinez-Mera et al. [27] proposed segmenting the thoracic aorta in contrast-enhanced CT angiography (CTA) images using a combination of level-set and region-growing algorithms. They use the Hough transform to locate the aorta and define region-growing seed points in the original image. The regions (aortic arch, descending aorta, and ascending aorta) were grown using the mean and variance of the neighbouring voxels. The level set method is then used to refine and segment the missing parts. Performance decreased in the heart region, where the boundaries with the contrast-filled cardiac chambers are blurred. Gamechi et al. [17] developed a fully automatic segmentation of the thoracic aorta from non-contrast-enhanced CT data.

Multi-atlas registration is used to localize the aorta, and seed points are placed in the ascending and descending aorta as the centers of mass of the initial aorta surface estimation. The aortic centerline is then extracted from the defined seed points. An optimal surface graph cut technique, initialized through a dilated centerline, is employed to extract the aortic surface. Trullo et al. [41] proposed a deep learning framework for joint segmentation of thoracic organs in CT images, specifically the aorta, heart, esophagus, and trachea. The approach used a SharpMask-based fully convolutional network (FCN) to combine low-level and high-level features for improved localization. The approach requires a large amount of labeled data for training, which is often not freely available in medical image processing.

This work presents a robust framework for segmenting the entire aorta (thoracic and abdominal aorta) from non-enhanced CT data. Our framework consists of three steps. First, we extract, from two given points, a path within the aorta using the minimal path approach [11]. Usually, the minimal path approach is applied to images with high contrast in the region of interest. However, we define a new potential function that combines image intensity and edge detection, making it applicable to our low-contrast input image data. In the second step, we utilize a 3D Lagrangian curve evolution model [33] to move the initial path toward the approximate centerline of the aorta. In the Lagrangian curve evolution, the motion of a given curve is defined by a vector field. In [33], the vector field is determined from the segmented colon. However, we do not have the segmented aorta. Therefore, we define a new vector field from the edge detector. In the third step, we utilize the centered path to construct the initial condition for the GSUBSURF method [29–31], which ultimately yields the final segmentation. The GSUBSURF provides satisfactory results when the initial segmentation is appropriate. For example, to segment a circular structure, a good initial condition is constructed from a point at the center of mass of the structure [38]. Therefore, we use the aorta centerline to build the initial condition. The contribution of this paper is to provide a complete framework for extracting the entire aorta from non-enhanced CT data. Each step of our framework is robust enough to handle the anatomical variability of the aortic shape and can segment the aorta from CT images, with or without contrast-enhanced material.

The paper is organized as follows: in Section 2, we present the extraction of a path within the aorta, and in Section 3, we present the centering of the extracted path. In Section 4, we present the GSUBSURF model and its application to aorta segmentation, discussing our segmentation results. In Section 5, we present the application of our segmentation framework to the diagnosis of large vessel vasculitis. In the final section, we conclude our work and emphasize the global implications of our study.

2. Path extraction within the aorta

In this section, we extract a path within the aorta using the minimal path approach. The minimal path approach was introduced in [11] as a global minimization formulation of the snake model [21] using the *Fast Marching* method [39]. It simplifies the initialization of the snake model by setting just two endpoints. The authors start by converting the snake energy into a path integral. Then, they define the minimal action map and show that its level-set propagation implies the Eikonal equation. They finally solved the Eikonal equation by the *Fast Marching* method and back-traced the solution to obtain the globally minimal path. In [11], the model was applied to road extraction in 2D aerial images and to organ segmentation in 2D medical images. The model has been extended to 3D in [16] for applications such as virtual endoscopy in medical images. Computational improvements, such as partial propagation starting from one endpoint and stopping at the second one, were introduced to make the model effective for real-time applications. In [6], the authors introduced another improvement: a single endpoint is specified and new points are automatically detected during front propagation. Each newly detected point is set as a new starting point to create a recursive growth path. This improvement enables the extraction of a path in an elongated 2D/3D structure. The authors [6, 11, 16, 25] noted that the quality of the extracted path depends strongly on the definition of the potential function. In noisy and complex 3D structures, such as the aorta in non-enhanced CT data, the paths may cross the vessel wall, leading to invalid paths. To overcome this issue, we introduce a potential function that allows the extraction of a path within the aorta in a single step. In cases of poor contrast, the growing approach is used to ensure that the path remains within the aorta.

2.1. Minimal path approach

Consider a parametric curve

$$\Gamma(v) : \Omega \to \mathbb{R}^3, \qquad v \mapsto \big(x(v), y(v), z(v)\big)$$

in a 3D image, where $\Omega = [0, 1]$ is the parameterization interval, and v is a parameter. For a space $\mathcal{A}$ of admissible paths Γ, the snake energy $E : \mathcal{A} \to \mathbb{R}$ has the following form

$$\Gamma \mapsto E(\Gamma) = \int_{\Omega} \Big(\frac{\omega_1}{2} ||\Gamma'(v)||^2 + \frac{\omega_2}{2} ||\Gamma''(v)||^2 + P\big(\Gamma(v)\big) \Big)\, dv, \tag{1}$$

where Γ', Γ'' are the first and second derivatives of Γ with respect to v, $||\cdot||$ is the Euclidean norm in $\mathbb{R}^3$, P is the potential function defined from the image, ω_1 and ω_2 are the model parameters [11, 21]. Contrary to the classical snake energy [21], the authors of [11], chose v as the arc-length parameter s, which means $||\Gamma'(s)|| = 1$, then $\Omega = [0, L]$, where L is the length of the curve.

This makes the energy depend only on the geometric curve and not on the parametrization [11]. The second derivative of Γ is removed from the energy (1). These changes yield a model in which initialization involves setting only two endpoints and the potential function responsible for curve smoothing. The energy of the new model $E : \mathcal{A}_{p_s,p_f} \to \mathbb{R}$ has the following form

$$\begin{aligned}\Gamma \mapsto E(\Gamma) &= \int_0^L \Big(\omega||\Gamma'(s)||^2 + P\big(\Gamma(s)\big)\Big) ds \\ &= \int_0^L \Big(\omega + P\big(\Gamma(s)\big)\Big)\, ds \\ &= \int_0^L \tilde{P}\big(\Gamma(s)\big)\, ds,\end{aligned} \tag{2}$$

where $\tilde{P} = \omega + P$ is defined from the image, $\mathcal{A}_{p_s,p_f}$ is the space of all curves connecting the starting point p_s and a final point p_f. The boundary conditions are given by

$$\Gamma(0) = p_s, \quad \text{and} \quad \Gamma(L) = p_f.$$

The parameter $\omega > 0$ is used to control the smoothness of the curve.

At each point p in the image domain, and for $\tilde{P} > 0$, the minimal action U_{p_s} corresponds to the minimal energy integrated along a path that starts at p_s and ends at p

$$U_{p_s}(p) = \inf_{\Gamma(L)=p} \left(\int_\Gamma \tilde{P} ds \right) = \inf_{\mathcal{A}_{p_s,p}} E(\Gamma). \tag{3}$$

$\mathcal{A}_{p_s,p}$ is the set of all the paths between p_s and p.

To compute the minimal action U_{p_s}, the authors of [11] formulated the following partial differential evolution equation (related to (3))

$$\frac{\partial \mathcal{L}(s,t)}{\partial t} = \frac{1}{\tilde{P}} \vec{n}(s,t) \tag{4}$$

for the set of equal energy isosurfaces $\mathcal{L}$ in "time"

$$\mathcal{L}(s,t) = \{p \in \mathbb{R}^3 \mid U_{p_s}(p) = t\}, \tag{5}$$

where $\vec{n}(s,t)$ is the normal to $\mathcal{L}(\cdot,t)$. The equation (4) is a front propagation equation with a speed $\frac{1}{\tilde{P}}$ where t represents the time at which the front passes over the point p in the image domain. It starts with an initial surface represented by a small sphere centered at the starting point p_s until U_{p_s} is computed for all points in the image domain. During front propagation, the head of the front moves faster in regions with smaller potential values $\tilde{P}$. We denote the head

of the front as the farthest point (in terms of the local norm) from the starting point reached by the front. In fact, the authors of [11] also showed that U_{p_s} satisfies the Eikonal equation

$$||\nabla U_{p_s}|| = \tilde{P}, \qquad U_{p_s}(p_s) = 0. \tag{6}$$

In this work, as in [11], we employ the *Fast Marching* method [39] to compute U_{p_s} because it is fast and has a lower computational complexity compared to other approaches [11,16].

The gradient of U_{p_s} is orthogonal to the propagating front. Therefore, the minimal path Γ_{p_s,p_f} between any point p_f and the starting point p_s can be found by back-propagation on the map U_{p_s}. To find Γ_{p_s,p_f}, the authors in [11,16] suggest the *Steepest Descent Gradient* method

$$p_{i+1} = p_i - \tau \frac{\nabla U_{p_s}}{||\nabla U_{p_s}||}, \quad \tau > 0, \quad i = 0, \ldots, M-1, \tag{7}$$

where τ is taken as $0 < \tau < 1$ and M is the maximal number of iterations. The algorithm starts with $p_0 = p_f$ and stops when the Euclidean distance between the current point p_i and p_s is less than a given tolerance.

2.2. Potential function

The potential function $\tilde{P}$ governs the evolution of the front in the *Fast Marching* front propagation. The definition of the potential function depends on the application. An effective potential exhibits strong contrast between the regions of interest, their boundaries, and the surrounding background. In practice, low potential values are assigned to pixels or voxels in the target region, whereas high values are assigned to background voxels [6,11,16]. With such a function $\tilde{P}$, we expect the front to reach regions of interest before spreading to less relevant regions, leading to the extraction of the expected path. However, erroneous paths may be extracted when the potential is noisy, insufficiently contrasted, or when the target structure is elongated, thin, or highly curved [6]. In segmentation tasks, for example, the potential function is typically designed to take smaller values along object boundaries [11]. In our application, in contrast, smaller values are assigned to voxels along the aorta centerline and larger values to voxels along the aorta walls, so the boundaries act as barriers confining the front within the aorta. In the following sections, I denotes the input image filtered by the geodesic mean curvature flow filtering [23]. For our application, we propose the following potential function

$$\tilde{P}(p) = \left(\omega + \frac{|\tilde{I}(p_s) - I(p)|}{\max\limits_{q \in \mathcal{I}} (|\tilde{I}(p_s) - I(q)|)} \right) \frac{1}{1 + d(p)}, \quad \forall p \in \mathcal{I}, \quad p \neq p_s, \tag{8}$$

where $\mathcal{I} \subset \mathbb{R}^d$, $d = 2, 3$, is the image domain, $\tilde{I}(p_s)$ is the mean image intensity value in a spherical volume centered at the starting point p_s, and $I(p)$ is the image intensity at the point $p \in \mathcal{I}$. The parameter $\omega > 0$ controls the smoothness of the path and is also used to avoid the term of (8) in parentheses being 0. The term in parentheses emphasizes voxels that differ from p_s. Voxels with image intensity similar to intensity in the p_s neighbourhood are assigned low values, whereas voxels from other regions, including boundaries, receive high values. The second term of (8) is a function of d, which is the distance map computed on the edge image. To obtain the edge image, we first compute the edge detector using the function

$$g(|\nabla I|) = \frac{1}{1 + K|\nabla I|^2}, \tag{9}$$

where $K > 0$. The function (9) is introduced in [37] for edge detection using anisotropic diffusion. A small value of the function (9) means weak diffusion, so the edges are preserved. The parameter K controls the edge sensitivity. Therefore, the edge image is a binary image B obtained by thresholding ($\delta > 0$)

$$\begin{cases} g\big(|\nabla I(p)|\big) < \delta \implies B(p) = 1, & (10) \\ g\big(|\nabla I(p)|\big) \geq \delta \implies B(p) = 0. & (11) \end{cases}$$

The voxels $p \in \mathcal{I}$ for which (10) holds are called edge voxels, and those for (11) are called background voxels. Using the *Fast Marching* method, the distance map assigns each background voxel a positive value equal to its shortest distance to the nearest edge voxel (which has a distance 0). Therefore, points (voxels) located at the aorta's centerline get a value approximately equal to the radius of the aorta. When the edges are perfectly detected, we obtain a centered path within the aorta in one step. However, in non-enhanced CT data, several regions of the aorta may exhibit weak or missing edges, and the edge image may not capture them. Therefore, combining these two terms globally yields small values within the aorta and large values at the edges. We used a similar potential function in a previous work [2]

$$\tilde{P}_{\text{prev}}(p) = \omega + \frac{|\tilde{I}(p_s) - I(p)|}{\max\limits_{q \in \mathcal{I}} (|\tilde{I}(p_s) - I(q)|)} \frac{1}{1 + d(p)}, \quad \forall p \in \mathcal{I}, \quad p \neq p_s. \tag{12}$$

Here, ω is added to the product of the two terms. The difference between the two potentials is based on the fact that, in this work, the smoothing effect of ω is reduced to favor the centering term (the term with distance). This change is essential because we have only two input points (in this work) and aim to extract a path within the aorta in a single step.

2.3. Minimal path approach with keypoints detection

During front propagation, when there are missing or weak edges, the front may flow outside the aorta, and other parts of the front may reach the specified final point before the front located within the aorta (see Fig. 6). This is an illustration of a shortcut, which occurs more often when the input data have low contrast, such as in non-enhanced CT images. One solution to overcome such shortcuts is to use the minimal path approach with keypoint detection [6]. The idea is to update the starting point during the front propagation, denoted as a keypoint along the path, before the front reaches the final point. In the *Fast Marching* front propagation, the computation of the action map U_{p_s} starts in the neighbourhood of the starting point p_s, and U_{p_s} is computed progressively for all the domain points. A keypoint is the first point p_k reached by the front for which

$$||p_s - p_k|| \geq \lambda, \tag{13}$$

where λ is a positive real number. The newly detected keypoint is defined as the new starting point. The process is repeated until the front reaches the final point (see Fig. 7). As the authors of [6] noted, the keypoint should be within the aorta because the front propagates faster where the potential is small, i.e., along the aorta's centerline. Too large λ (larger than the distance between the aortic root and the descending aorta) may not solve the shortcut problem in the thoracic region. Therefore, the choice of λ should consider the curved shape of the aortic arch, as it is the region where the shortcut occurs more frequently. If λ is too large, the front propagates for a longer time before finding a new keypoint, potentially passing through regions with missing edges, thus increasing the risk of finding the keypoint outside the aorta. The optimal parameter λ is found after an intensive search, as the length and shape of the aorta vary from one patient to another.

2.4. Numerical experiments

In this section, we present path extraction using our proposed potential (8) in both artificial and real images. The objective is to highlight the improvements implied by $\tilde{P}$ compared to the potentials used in the literature [16], such as

$$P_{\text{ref}} = \omega + |\tilde{I}(p_s) - I(p)|, \tag{14}$$

where $\tilde{I}(p_s)$ can be either the mean of the image intensity values in a neighbourhood of p_s, the mean image intensity values in the starting and final points, or the mean of the image intensity values in the region of interest (see [16]).

2.4.1. Artificial data

In the original snake energy [21], the location of the initial curve is crucial to obtain the expected curve. Energy minimization can become trapped in local minima, leading to a shortcut. The authors in [11] introduced the new snake energy (2) to achieve a global minimum, thus reducing the likelihood of shortcuts. However, shortcuts may still occur when the potential $\tilde{P}$ is not sufficiently contrasted or when the regularization parameter ω is too large (see the red curve in Fig. 2). They suggested tuning ω to avoid shortcuts. In [16], for tubular structures, shortcuts lead to a path that is tangent to the boundaries rather than centered (see the blue curve in Fig. 2). To obtain the centered path, they first segment the structure of interest and then use a distance-to-edge-based potential to derive it. Our proposed potential $\tilde{P}$ combines these two steps, resulting in a centered path when the edges are correctly extracted.

In Fig. 2, we present an example where the structure of interest is a 3D spiral-like structure. The object voxel values are set to 0.8, and the background voxels are set to 0.7. Using the potential P_{ref}, the regularization parameter $0 < \omega < 0.05$, and $\tilde{I}(p_s)$ taken as the mean of the object voxel intensity values in the neighbourhood of the starting point p_s, we obtain the blue path, which is not centered and tangent to the boundaries. When $\omega \geq 0.05$, the shortcut occurs, and we obtain a wrong path (red). For $0 < \omega < 0.05$ and using $\tilde{P}$ (8), we get a centered path (green) in a single step.

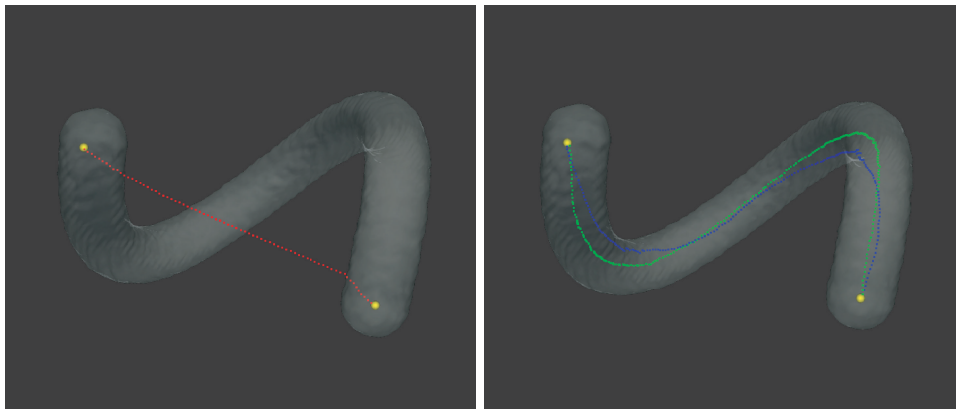

FIGURE 2. Paths extraction within complex 3D shape. The yellow dots are the endpoints. The red path is incorrect due to a shortcut. The blue path is located within the structure, but it is not centered, and the green path is centered.

In Fig. 3, we present the result of the path extraction using the object in the previous example, but with missing parts of the object's boundaries. In the first case, we create a hole in the middle of the object and another hole near the final point. The second has just one hole in the middle of the object. The distance to the edge term in $\tilde{P}$ (8) decreases the potential value for all the voxels farther away from the object edges. Therefore, the front (during propagation) flows out of the structure through the region with missing edges (hole), potentially leading to an incorrect path.

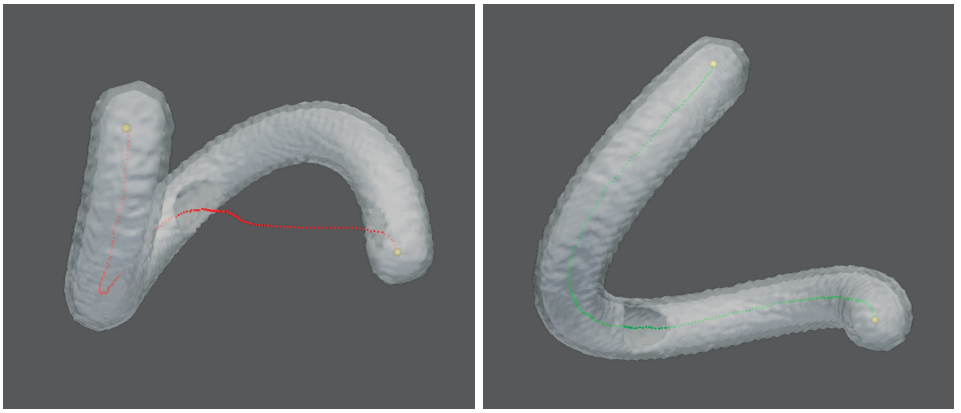

FIGURE 3. Extracted path with missing edges near endpoints (red) and far away from the endpoints (green).

The example in Fig. 3 demonstrates that we can still extract the expected path even when a few edges are missing and the endpoints are chosen within a region with complete edges. The case in which edges are missing in many regions can be addressed using the growing approach. We will illustrate these cases using real data experiments.

2.4.2. Real data

The datasets are provided by BIONT a.s. in Bratislava. The image data are acquired for patients suspected of having vasculitis. Each data set comprises 3D CT and PET images in the same coordinate system. The CT image data consist of a sequence of 2D slices. The slice resolution is 512×512. In CT images, each voxel is assigned a numerical value (intensity) corresponding to the average X-ray attenuation within the voxel, expressed in Hounsfield Units (HU). Our datasets consist of data from six patients. Patients 1 and 2 correspond to data from the same patient, except that the scans were performed one year apart. In fact, the images' origins and the number of slices in the 3D volumes

differ, so the images cannot be compared without primary processing. Given the limited data available, we treat them as two separate patients. The information about the CT data in our datasets is summarized in the following table

TABLE 1. Information of CT data for patient 1 (P1) to patient 6 (P6).

		P 1	P 2	P 3	P 4	P 5	P 6
Intensity (HU)	min	-1024	-1024	-3024	-3024	-1024	-1024
	max	2976	2976	3071	3071	3071	3071
Spacing (mm)	s_x	1.172	1.172	0.977	0.977	0.977	0.977
	s_y	1.172	1.172	0.977	0.977	0.977	0.977
	s_z	2.5	2.5	2.5	2.5	1.5	1.5

To use similar parameters, we rescale the input data to the range $[0, 1]$. We apply geodesic mean curvature flow filtering [23] as a preprocessing step to remove noise while preserving edges. The endpoints for the path extraction are set manually. The edge image threshold is set to 0.2 for patients 1 and 2 and to 0.25 for patients 3 to 6. For strong edges, a small threshold is used to obtain the edge image. However, for weak edges, we need to increase the threshold to capture more edges. The regularization parameter ω is set proportional to the standard deviation of the voxel intensities within a small neighbourhood of the starting point p_s.

The 3D PET data have lower resolution (compared to CT) and consist of a sequence of 2D slices. The slice resolution

for Patients 1 and 2 is 144×144,

for Patients 3 and 4 is 128×128, and

for Patients 5 and 6 is 220×220.

The information about the spacings is summarized in the following table

TABLE 2. Information of PET data for patient 1 (P1) to patient 6 (P6).

		P 1	P 2	P 3	P 4	P 5	P 6
Spacing (mm)	s_x	4	4	3.91	3.91	3.3	3.3
	s_y	4	4	3.91	3.91	3.3	3.3
	s_z	4	4	4.25	4.25	3	3

Fig. 4 illustrates how the proposed potential values $\tilde{P}$ (8) are small in the aorta region. This is our expectation: the front propagates into the aorta before the other regions.

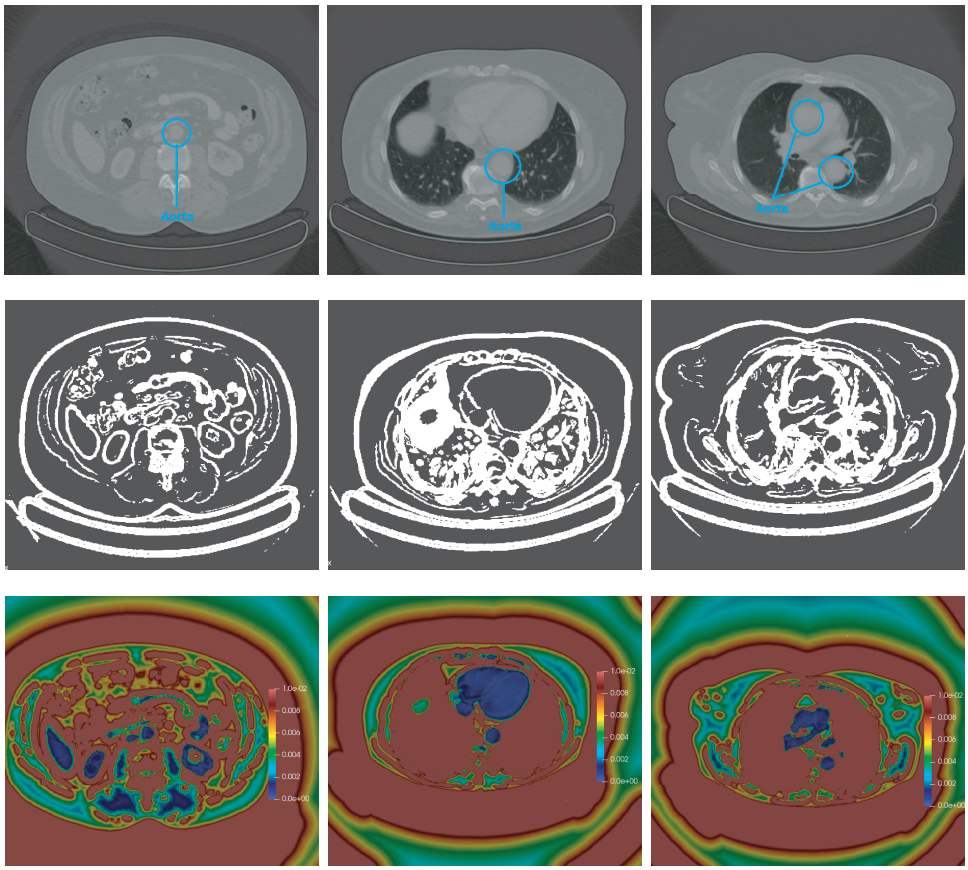

FIGURE 4. The first row shows three different axial views of the CT images where the aorta is visible (blue circles). The second row shows the edge image computed from the previous input slices. The third row shows the potential function corresponding to each slice. The slices are extracted from the 3D volume of Patient 1.

Fig. 5 illustrates the extracted paths in a single step for two patients using the proposed potential $\tilde{P}$ (8). For the potential P_{ref} and various sets of parameters ω, $\tilde{I}(p_s)$, we were unable to obtain the expected path in one single step. However, when using the potential $\tilde{P}$, the expected paths are extracted for four out of the six patients. That means that the potential $\tilde{P}$ improves the potential P_{ref}, which is defined with only voxel intensity values. The advantage of the proposed potential $\tilde{P}$ is that it performs well even in regions with weak edges when

the threshold for the edge image is adjusted. A thorough investigation of the patient data, which revealed incorrect paths, indicates that these shortcuts occur in regions with high curvature and missing edges. To overcome this shortcut issue, we employ the growing minimal path approach to obtain the expected paths.

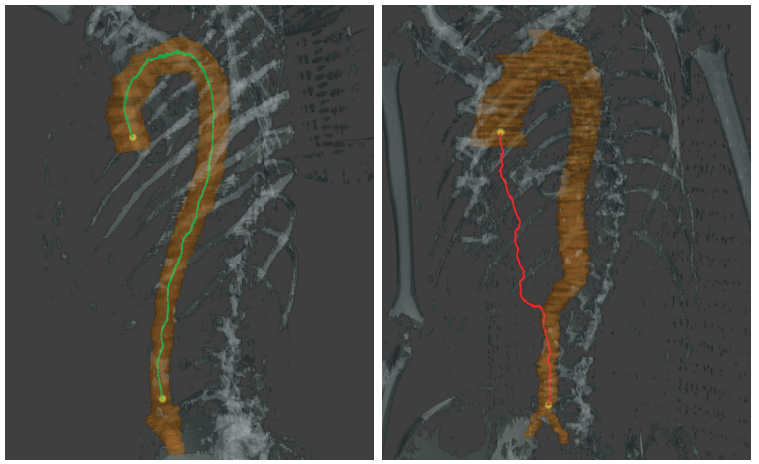

FIGURE 5. Extracted paths for patients 4 and 5. The aorta (orange) is segmented manually for visualisation purposes. The yellow dots are the starting and final points. The green path is the expected path for patient 4 using the potential $\tilde{P}$, and the red path is an incorrect path for patient 5 due to a shortcut.

The Fig. 6 presents the evolution of the front from the starting point to the final point. Since the aorta is long with some missing edges, the front flows outside, reaching the final point before the front inside the aorta reaches the final point. This is a typical illustration of a shortcut when the potential is not sufficiently contrasted, and the structure of interest is long.

Fig. 7 shows the front evolution with keypoints detection for $\lambda = 50$.

Fig. 8 shows the extracted paths for our datasets using the minimal path approach with keypoints detection (see section 2.3). This approach allows us to overcome the shortcut issue observed earlier. All the keypoints are found within the aorta (for all patients) using the same $\lambda = 50$. However, keypoints are sometimes found outside the aorta when the previous keypoint is close to an edge or in regions with weak or missing edges. For our dataset, this situation occurs more frequently in the heart region. Therefore, the challenge with this approach is to define λ so that we detect all keypoints within the aorta. The authors of [10] introduced a solution to the problem. Their idea is to use a path score

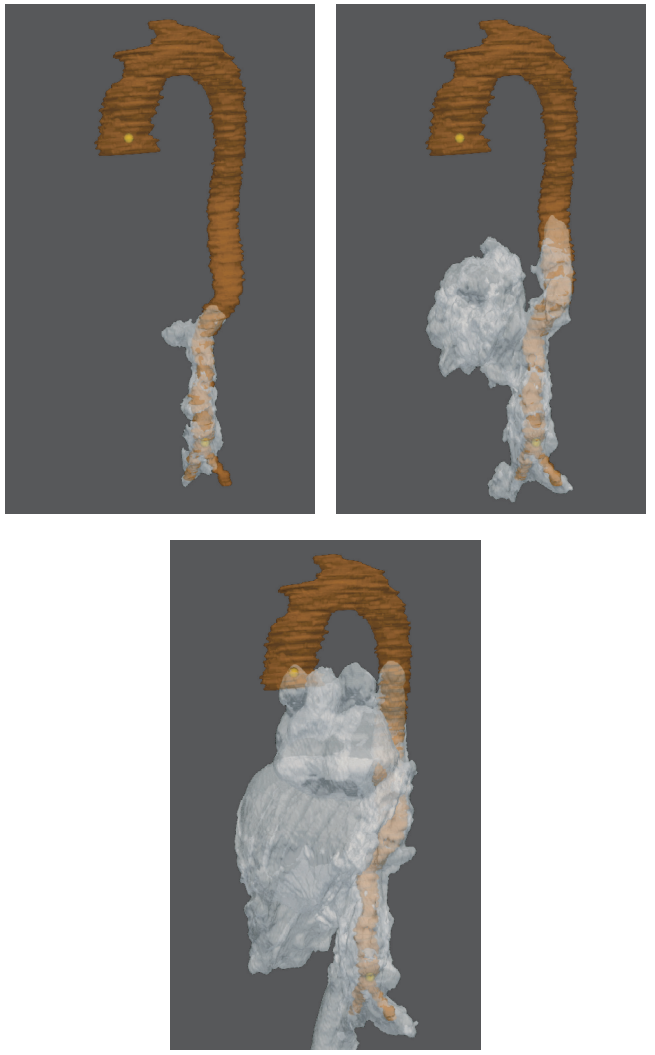

FIGURE 6. Three steps of the evolution of the front from the starting point to the final point for patient 5. It corresponds to the action map U_{ps} used to extract the red path in Fig. 5.

to select the candidate keypoint and use an anisotropic potential to keep finding keypoints in the target region. For the anisotropic potential, an anisotropic *Fast Marching* method [36] is required, which has computational complexity $\mathcal{O}(N\ ln\ N + N\ ln\ \kappa(\mathcal{M}))$ versus $\mathcal{O}(N\ ln\ N)$ for the isotropic (classical) *Fast Marching* [39]. The constant N is the number of voxels in the image, $\kappa(\mathcal{M})$ the maximum anisotropy ratio, and $\mathcal{M}$ a symmetric definite positive matrix that encodes the desired anisotropy at a given point. Since our path extraction is

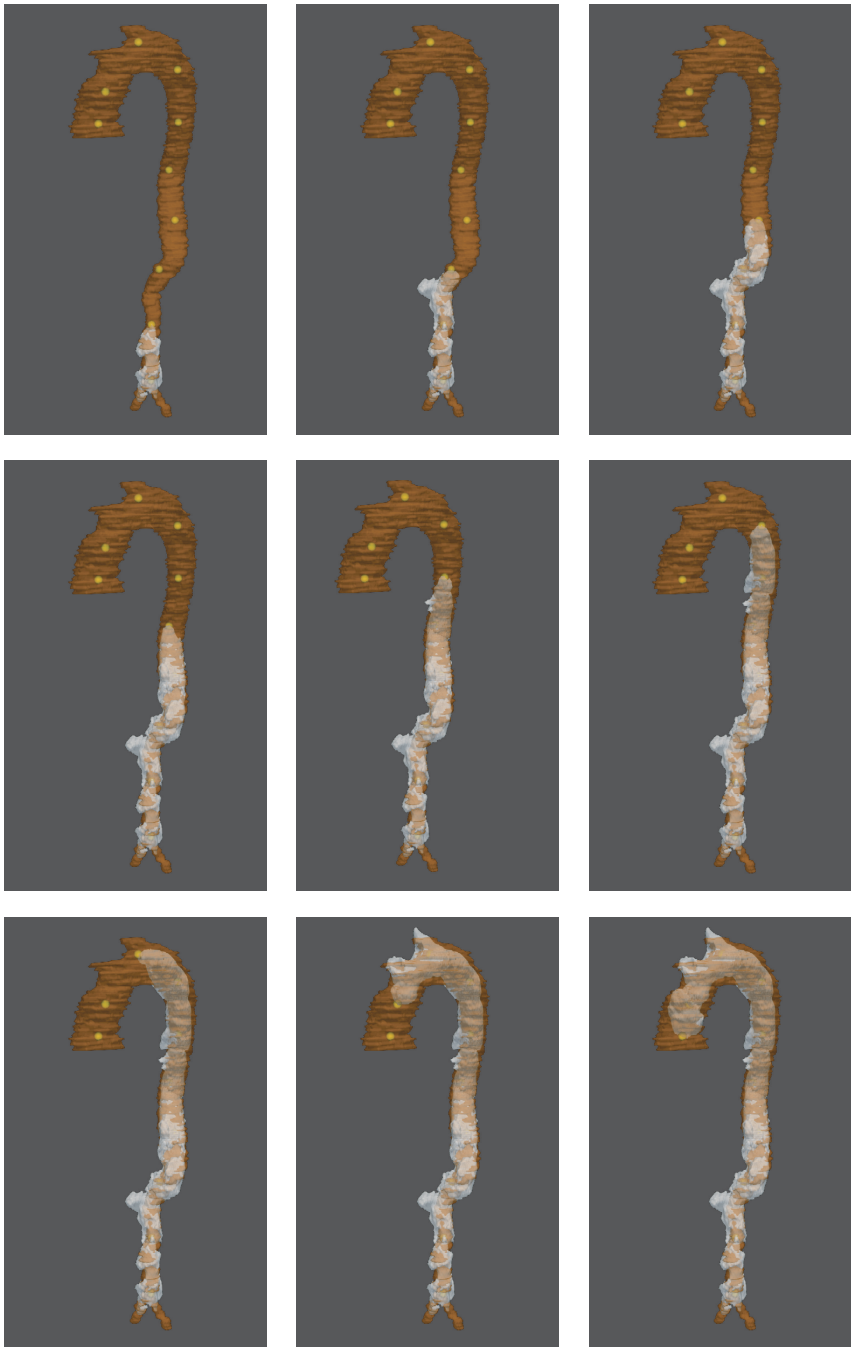

FIGURE 7. Front propagation with keypoints detection for patient 5. The detected keypoints are the yellow dots and $\lambda = 50$.

a step in a comprehensive framework for real-time applications, we employ the original approach and search for the optimal λ experimentally.

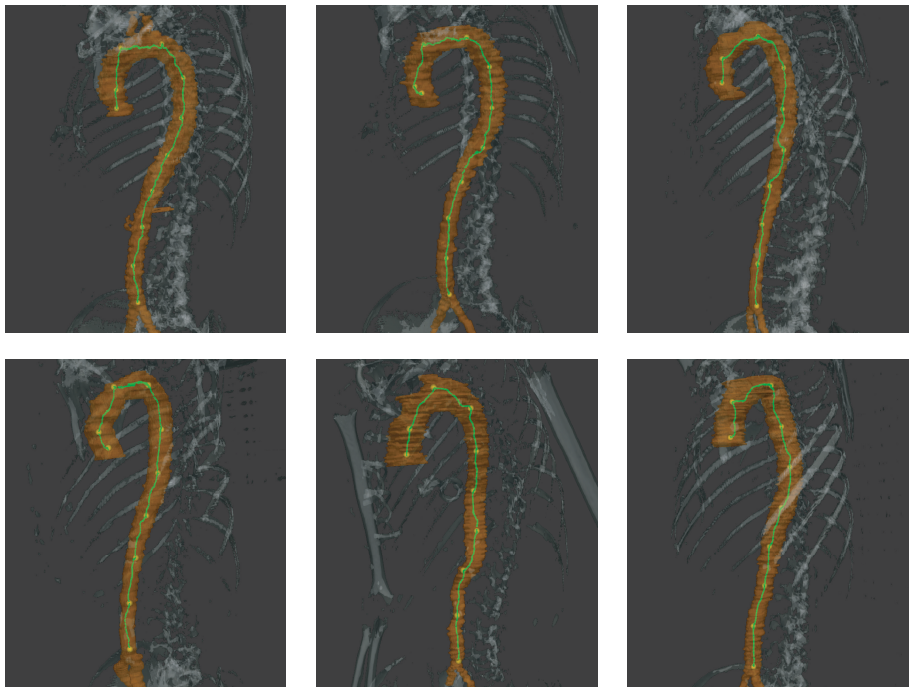

FIGURE 8. Extracted paths using the growing minimal path approach. Patients 1 to 3 in the first row and patients 4 to 6 in the second row. The yellow dots are the keypoints and $\lambda = 50$.

3. Path centering

The objective in the previous section was to extract a centered path in one single step to construct an appropriate initial condition for the GSUBSURF segmentation. Unfortunately, due to missing or weak edges, it is sometimes required to employ the growing minimal path approach to extract a path within the aorta. The extracted path is not centered because the keypoints are sometimes close to the edges (see the first image in row 2 of Fig. 8). In this section, we move the extracted path to the approximate centerline of the aorta. Our application is based on the 3D Lagrangean curve evolution presented by Mikula and Urbán in [33]. The model moves a 3D curve smoothly in the normal plane within a complex tubular structure.

3.1. Mathematical model

Let $\Gamma : [0,1] \to \mathbb{R}^3$, $\Gamma = \{\mathbf{r}(t,u), u \in [0,1]\}$ be an open curve depending on time t and let $\mathbf{r}(t,u) = \big(x(t,u), y(t,u), z(t,u)\big)$ be a position vector of the curve Γ for the parameter u in time t. The discretized curves are represented by sets of 3D points $\mathbf{r}_i^n = (x_i^n, y_i^n, z_i^n)$, where $i = 0, \ldots, m$, is the grid points number, and n represents the time step. Our input curves are the paths extracted in the previous section (see Fig. 8).

The motion of a curve in a general vector field $\mathbf{v}$ can be described by the following model

$$\partial_t \mathbf{r} = \mathbf{v}(\mathbf{r}). \tag{15}$$

For a given tubular structure, the distance to the edge inside the structure has a ridge along the centerline, and the gradient of that distance function points towards the ridge. In [33], the structure of interest is the colon, so the authors compute the distance map using the segmented colon. Contrary to what was done in [33], we do not have a segmented aorta as input, so we use edge detection to extract the aorta edges. Then we threshold the edge detector to obtain an edge image where the aorta edges are visible (see Sect. 2.2). Therefore, an edge image with "good enough" aorta edges is a good input for the distance function. Various approaches can be employed to compute the distance map, including *Fast Sweeping* [45], *time-relaxed Rouy-Tourin* [33], and *Fast Marching* [39]. *Fast sweeping* is the quickest approach, but it is also the least precise. The *time--relaxed Rouy-Tourin* and *Fast Marching* show similar precision, but the *Fast Marching* is much quicker. Therefore, we employ the *Fast Marching* method, which solves

$$|\nabla d| = 1 \tag{16}$$

to compute the distance map. The velocity vector field $\mathbf{v}$, for the curve evolution, is thus given by

$$\mathbf{v} = \nabla d. \tag{17}$$

The curve evolution model is based on the solution of the following partial differential equation [33]

$$\partial_t \mathbf{r} = \mu\ \mathbf{N}_\mathbf{v} + \varepsilon\ k\mathbf{N} + \alpha\ \mathbf{T}, \tag{18}$$

where $k\mathbf{N}$ is the curvature vector, α the tangential velocity, $\mathbf{T}$ the unit tangent vector to the curve, μ and ε are parameters. The projection of the velocity vector field $\mathbf{v}$ to the curve's normal plane is given by

$$\mathbf{N}_\mathbf{v} = \mathbf{v} - (\mathbf{T} \cdot \mathbf{v})\mathbf{T}, \tag{19}$$

i.e., the tangential component of $\mathbf{v}$ is removed, and the motion in the curve normal plane is regularized by the curvature term. To ensure uniform curve discretization, a new tangential velocity α is added to the model. Since $\mathbf{T} = \partial_s \mathbf{r}$ and $k\mathbf{N} = \partial_{ss}\mathbf{r}$, the advection-diffusion form of (18) is given by

$$\partial_t \mathbf{r} = \mu\ \mathbf{N}_\mathbf{v} + \varepsilon\ \partial_{ss}\mathbf{r} + \alpha\ \partial_s \mathbf{r}. \tag{20}$$

The Dirichlet boundary condition is applied to the model (i.e., the first and last points are fixed). The normal component of the (new) velocity vector field moves the curve points toward the object ridge, and the tangential component uniformly redistributes the points along the curve [33].

In order to define a suitable tangential velocity α, we consider the local orthogonal basis $(\mathbf{T}, \mathbf{N}_1, \mathbf{N}_2)$ that smoothly vary along the curve [33]

$$\mathbf{N}_1 = \frac{\mathbf{N_v}}{|\mathbf{N_v}|}, \qquad \mathbf{N}_2 = \mathbf{N}_1 \times \mathbf{T}.$$

If $|\mathbf{N_v}| = 0$, then $\mathbf{N}_1$ is replaced by the normalized mean of the neighbouring normal vectors. The projections of the curvature vector $k\mathbf{N}$ onto $\mathbf{N}_1$ and $\mathbf{N}_2$ are given by

$$k_1 = k\mathbf{N} \cdot \mathbf{N}_1, \qquad k_2 = k\mathbf{N} \cdot \mathbf{N}_2,$$

then the curvature vector satisfies

$$k\mathbf{N} = k_1\mathbf{N}_1 + k_2\mathbf{N}_2$$

and the equation (20) can be written as [33]

$$\partial_t \mathbf{r} = U\mathbf{N}_1 + V\mathbf{N}_2 + \alpha\mathbf{T}, \tag{21}$$

where the normal components are given by

$$U = \varepsilon k_1 + \mu|\mathbf{N_v}|, \qquad V = \varepsilon k_2.$$

The suitable tangential velocity α satisfies [33]

$$\partial_s \alpha = Uk_1 + Vk_2 - < Uk_1 + Vk_2 >_\Gamma + \left(\frac{L}{g} - 1\right)\omega_r, \tag{22}$$

where g is the local segment length, L the total length of the curve, $< \cdot >_\Gamma$ the arc-length average and ω_r is the redistribution rate. The choice of ω_r makes the quantity $\theta = ln(\frac{g}{L})$ converge to 0, which means an asymptotically uniform spacing between the curve points [33].

3.1.1. Discretization

The discretization follows the flowing finite volume method [33–35]. Let

$$h_i^n = |\mathbf{r}_i^n - \mathbf{r}_{i-1}^n|$$

be the primal arc lengths and

$$\left|\mathbf{r}_{i-\frac{1}{2}}^n - \mathbf{r}_{i+\frac{1}{2}}^n\right| = \frac{h_i^n + h_{i+1}^n}{2}$$

be the dual segment length at a given time n. The time derivative $\partial_t \mathbf{r}$ is

approximated by a forward finite difference and integrated over the dual segment (finite volume)

$$\int_{\mathbf{r}^n_{i-\frac{1}{2}}}^{\mathbf{r}^n_{i+\frac{1}{2}}} \partial_t \mathbf{r}\ ds = \frac{h^n_{i+1} + h^n_i}{2}\ \frac{\mathbf{r}^{n+1}_i - \mathbf{r}^n_i}{\tau}, \tag{23}$$

where τ is the time step.

The normal component of the velocity field $\mu\mathbf{N_v}$ is approximated explicitly and integrated over the dual segment

$$\int_{\mathbf{r}^n_{i-\frac{1}{2}}}^{\mathbf{r}^n_{i+\frac{1}{2}}} \mu(\mathbf{N_v})^n_i\ ds = \mu\,\frac{h^n_{i+1} + h^n_i}{2}\,(\mathbf{N_v})^n_i. \tag{24}$$

The curvature term $\varepsilon\partial_{ss}\mathbf{r}$ is approximated implicitly and integrated over the dual segment

$$\begin{aligned}\int_{\mathbf{r}^n_{i-\frac{1}{2}}}^{\mathbf{r}^n_{i+\frac{1}{2}}} \varepsilon\partial_{ss}\mathbf{r}^{n+1}\ ds &= \varepsilon\left[\partial_s\mathbf{r}^{n+1}\right]_{\mathbf{r}^n_{i-\frac{1}{2}}}^{\mathbf{r}^n_{i+\frac{1}{2}}} \\ &= \varepsilon\left(\frac{\mathbf{r}^{n+1}_{i+1} - \mathbf{r}^{n+1}_i}{h^n_{i+1}} - \frac{\mathbf{r}^{n+1}_i - \mathbf{r}^{n+1}_{i-1}}{h^n_i}\right).\end{aligned} \tag{25}$$

Integrating the advection term $\alpha\partial_s\mathbf{r}$ over the dual segment, we obtain

$$\begin{aligned}\int_{\mathbf{r}_{i-\frac{1}{2}}}^{\mathbf{r}_{i+\frac{1}{2}}} \alpha\partial_s\mathbf{r}\ ds &= \alpha_i\left(\mathbf{r}_{i+\frac{1}{2}} - \mathbf{r}_{i-\frac{1}{2}}\right) \\ &= \frac{\alpha_i}{2}(\mathbf{r}_{i+1} - \mathbf{r}_{i-1}) \\ &= -\frac{\alpha_i}{2}(\mathbf{r}_i - \mathbf{r}_{i+1}) + \frac{\alpha_i}{2}(\mathbf{r}_i - \mathbf{r}_{i-1}).\end{aligned} \tag{26}$$

We consider the inflow velocity of advection α through the dual segment boundary $\mathbf{r}_{i-\frac{1}{2}}$ and the outflow through $\mathbf{r}_{i+\frac{1}{2}}$ [3, 28]

$$b^{\text{in}}_{i-\frac{1}{2}} = \max(-\alpha_i, 0), \qquad b^{\text{out}}_{i-\frac{1}{2}} = \min(-\alpha_i, 0), \tag{27}$$

$$b^{\text{in}}_{i+\frac{1}{2}} = \max(\,\alpha_i,\,0\,), \qquad b^{\text{out}}_{i+\frac{1}{2}} = \min(\,\alpha_i,\,0\,), \tag{28}$$

then the advection term (26) can be written as

$$-\frac{1}{2}\left(b^{\text{in}}_{i+\frac{1}{2}} + b^{\text{out}}_{i+\frac{1}{2}}\right)(\mathbf{r}_i - \mathbf{r}_{i+1}) - \frac{1}{2}\left(b^{\text{in}}_{i-\frac{1}{2}} + b^{\text{out}}_{i-\frac{1}{2}}\right)(\mathbf{r}_i - \mathbf{r}_{i-1}). \tag{29}$$

For the time discretization of the advection term, the inflow part is taken implicitly, and the outflow part explicitly, then (29) becomes

$$-\frac{1}{2}b^{\text{in}}_{i+\frac{1}{2}}\left(\mathbf{r}^{n+1}_i-\mathbf{r}^{n+1}_{i+1}\right)-\frac{1}{2}b^{\text{in}}_{i-\frac{1}{2}}\left(\mathbf{r}^{n+1}_i-\mathbf{r}^{n+1}_{i-1}\right)$$
$$-\frac{1}{2}b^{\text{out}}_{i+\frac{1}{2}}\left(\mathbf{r}^{n}_i-\mathbf{r}^{n}_{i+1}\right)-\frac{1}{2}b^{\text{out}}_{i-\frac{1}{2}}\left(\mathbf{r}^{n}_i-\mathbf{r}^{n}_{i-1}\right). \tag{30}$$

The discrete curvature vector is given by

$$(k\mathbf{N})^n_i=\frac{2}{h^n_{i+1}+h^n_i}\left(\frac{\mathbf{r}^n_{i+1}-\mathbf{r}^n_i}{h^n_{i+1}}-\frac{\mathbf{r}^n_i-\mathbf{r}^n_{i-1}}{h^n_i}\right) \tag{31}$$

and using the following approximation for the tangential unit vector

$$\mathbf{T}^n_i=\frac{\mathbf{r}^n_{i+1}-\mathbf{r}^n_{i-1}}{h^n_{i+1}+h^n_i} \tag{32}$$

we compute the quantities

$$(\mathbf{N}_1)^n_i,\ (\mathbf{N}_2)^n_i,\ k^n_{1i},\ k^n_{2i},\ U^n_i,\quad \text{and}\quad V^n_i.$$

The approximation of the tangential velocity α^n_i is obtained by intergrating (22) over the dual segment, and we obtain

$$\alpha^n_i=\alpha^n_{i-1}+h^n_i(U^n_ik^n_{1i}+V^n_ik^n_{2i})-h^n_i<Uk_1+Vk_2>^n_\Gamma+\left(\frac{L^n}{m}-h^n_i\right)\omega_r \tag{33}$$

for $i=1,\ldots,m-1$, setting $\alpha^n_0=0$ and getting $\alpha^n_m=0$.

The approximation of the PDE) (20) by a flowing semi-implicit finite volume scheme is then obtained by combining the formulas 23, 24, 25, and 30. Thus, it can be written as

$$\mathcal{A}^n_i\ \mathbf{r}^{n+1}_{i-1}+\ \mathcal{B}^n_i\ \mathbf{r}^{n+1}_i+\ \mathcal{C}^n_i\ \mathbf{r}^{n+1}_{i+1}=\mathcal{F}^n_i, \tag{34}$$

where the coefficients $\mathcal{A}^n_i$, $\mathcal{B}^n_i$, $\mathcal{C}^n_i$, and $\mathcal{F}^n_i$ are given by

$$\mathcal{A}^n_i=-\frac{\varepsilon}{h^n_i}-\frac{1}{2}b^{\text{in}}_{i-\frac{1}{2}},\qquad \mathcal{C}^n_i=-\frac{\varepsilon}{h^n_{i+1}}-\frac{1}{2}b^{\text{in}}_{i+\frac{1}{2}}, \tag{35}$$

$$\mathcal{B}^n_i=\frac{h^n_i+h^n_{i+1}}{2\tau}-(\mathcal{A}^n_i+\mathcal{C}^n_i), \tag{36}$$

$$\mathcal{F}^n_i=\frac{h^n_i+h^n_{i+1}}{2\tau}\mathbf{r}^n_i+\mu(\mathbf{N_v})^n_i\frac{h^n_i+h^n_{i+1}}{2}-\frac{1}{2}b^{\text{out}}_{i+\frac{1}{2}}(\mathbf{r}^n_i-\mathbf{r}^n_{i+1})$$
$$-\frac{1}{2}b^{\text{out}}_{i-\frac{1}{2}}(\mathbf{r}^n_i-\mathbf{r}^n_{i-1}). \tag{37}$$

Equation (34) represents three tridiagonal systems for the x, y, and z coordinates of the grid points $\mathbf{r}^n_i$, which represent the evolving curve points and can be solved by the Thomas algorithm.

3.1.2. Results

In this section, we present the results of the evolution of the extracted paths (all six patients) using the edge image to construct the velocity vector field $\mathbf{v}$.

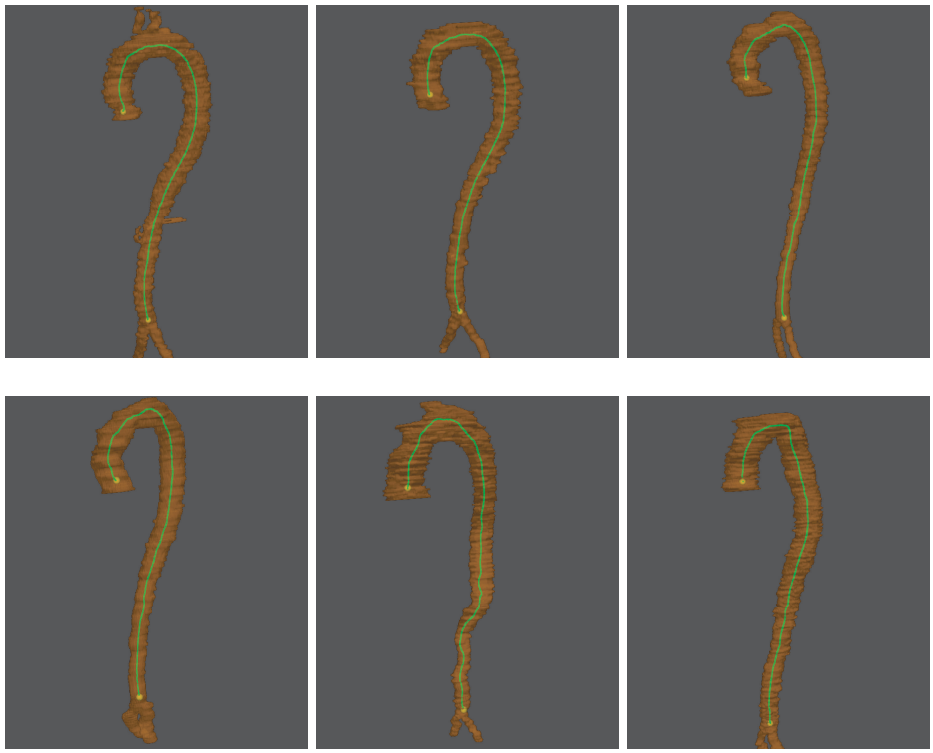

FIGURE 9. Centered paths (green) for six different patients. Patients 1 to 3 in the first row and patients 4 to 6 in the second row. The aorta (orange) is segmented manually for visualization purposes.

Fig. 9 shows the results of the curve evolution model applied to the paths extracted in the previous section. We stop the evolution when the total curve length no longer changes. We used the following parameters

$$\varepsilon = \mu = \omega_r = 1.$$

For the edge image, $K = 1000$ for all patients, and the thresholds are set to $\delta = 0.20$ for patients 1 and 2, and $\delta = 0.25$ for patients 3 to 6. When adjusting the threshold value for the edge image, we observed that the path is not perfectly centered in certain regions, where the edges are not accurately captured.

In contrast, the path remains well centered in regions where edge detection is reliable. These results demonstrate that the model [33] exhibits robustness in handling incomplete or missing edge information within the structure of interest.

4. The GSUBSURF model to segment the aorta

Let $I : \mathcal{I} \subset \mathbb{R}^3 \to \mathbb{R}$, represent the image to be segmented. The generalized subjective surface (GSUBSURF) model consists of defining an initial condition and letting it evolve according to the following advection-diffusion partial differential equation [29–31]

$$u_t - w_{\text{ad}}\ \nabla g \cdot \nabla u - w_{\text{dif}}\ |\nabla u|\ g\ \nabla \cdot \left(\frac{\nabla u}{|\nabla u|} \right) = 0, \tag{38}$$

where $u(.,t)$ is the segmentation function, $g(s) = \frac{1}{1+Ks^2}$ is an edge detector function, $K > 0$ is used to control the edge detection sensibility, and $s = |\nabla I|$. The image I is filtered with the geodesic mean curvature flow filter to remove noise and preserve the edges [23]. The parameters $w_{\text{ad}}, w_{\text{dif}} \in \mathbb{R}$ are used to control the advection and diffusion parts of the model. The velocity vector field $\mathbf{v} = -w_{\text{ad}} \nabla g$ is important, as it points toward the edges. The advection term moves the initial curve toward the edges, while the diffusion term handles the changes in the curve shape during evolution. We solve the problem in the domain $\mathcal{I} \times [0, T]$ and use the following boundary and initial conditions

$$u(p,t) = 0, \ \ \forall p \in \partial\mathcal{I}, \quad \text{and} \quad u(p,0) = u^0(p).$$

4.1. Initial segmentation function

The initial segmentation function is typically defined by a peak located approximately at the center of gravity of the object to be segmented [29, 31]. Therefore, we use the aorta's approximate centerline extracted in the previous section to construct the initial condition

$$u^0(p) = \frac{1}{1 + d(p)}, \quad p \in \mathcal{I} \subset \mathbb{R}^3, \tag{39}$$

where $d(p)$ is the minimal distance between p and the input curve Γ.

4.2. Finite volume space discretization

We consider a rectangular finite volume that corresponds to a voxel in the input image (see Table 1). We denote p as the current finite volume and

$$N(p) = \{e, w, n, s, t, b\}$$

as the set of its neighbours. The finite volume size is defined by the spacing in each direction h_x, h_y, and h_z. Let $m(p)$ denote the volume of the finite volume p, $m(p) = h_x h_y h_z$. We denote by e_{pq} the common boundary for two adjacent finite volumes p and q, with area $m(e_{pq}) = h_x h_y$ for the plane (x, y), $m(e_{pq}) = h_x h_z$ for the plane (x, z) and $m(e_{pq}) = h_y h_z$ for the plane (y, z). The edge connecting the centers of the current finite volume p and a given neighbour q is denoted σ_{pq}, and $m(\sigma_{pq})$ measures the edge length with

$$m(\sigma_{pq}) \in \{h_x, h_y, h_z\}.$$

We denote $\mathbf{v} = -w_{\mathrm{ad}} \nabla g$ and consider the transformation

$$\nabla \cdot (\mathbf{v}u) = u \nabla \cdot \mathbf{v} + \mathbf{v} \cdot \nabla u \implies \mathbf{v} \cdot \nabla u = \nabla \cdot (\mathbf{v}u) - u \nabla \cdot \mathbf{v}. \tag{40}$$

Integrating (38)) over the finite volume p, we get

$$\underbrace{\int_p u_t \, dp}_{\text{(I)}} + \underbrace{\int_p \nabla \cdot (\mathbf{v}u) dp - \int_p u \nabla \cdot \mathbf{v} dp}_{\text{(II)}} - \underbrace{\int_p w_{\mathrm{dif}} |\nabla u| g \nabla \cdot \left(\frac{\nabla u}{|\nabla u|} \right) dp}_{\text{(III)}} = 0. \tag{41}$$

Since the solution in the finite volume p is assumed to be constant u_p, after applying Green's theorem, (II) can be written as

$$\text{(II)} \approx \sum_{q \in N(p)} \int_{e_{pq}} u_{pq} \mathbf{v} \cdot n_{pq} \, ds - u_p \sum_{q \in N(p)} \int_{e_{pq}} \mathbf{v} \cdot n_{pq} \, ds, \tag{42}$$

where n_{pq} denotes the outer normal to the boundaries of finite volume p. The solution on the interface e_{pq} is denoted by u_{pq}. The integrated flux through a voxel face is given by [32]

$$v_{pq} = \int_{e_{pq}} \mathbf{v} \cdot n_{pq} \, ds = \int_{e_{pq}} - w_{\mathrm{ad}} \nabla g \cdot n_{pq} \, ds \approx -w_{\mathrm{ad}} G_{pq} m(e_{pq}), \tag{43}$$

where G_{pq} represents the approximation of the gradient of g on the interface e_{pq} (the explicit definition of G_{pq} is provided at the end of this section).

Using the integral fluxes, we define the inflows and the outflows through voxel faces [28, 31, 32], then we get

$$\text{(II)} \approx \sum_{q \in N(p)} \min(v_{pq}, 0)(u_q - u_p). \tag{44}$$

Applying Green's theorem to (III), we obtain

$$\text{(III)} \approx w_{\mathrm{dif}} \, |\nabla u_p| \, g_p \sum_{q \in N(p)} m(e_{pq}) \, \frac{1}{|\nabla u_{pq}|} \frac{u_q - u_p}{m(\sigma_{pq})}. \tag{45}$$

4.3. Time discretization

The term (I) is approximated by forward finite differences

$$\text{(I)} \approx \frac{u_p^{n+1} - u_p^n}{\tau} m(p). \tag{46}$$

The advection term (II) is implicitly approximated in time

$$\text{(II)} \approx \sum_{q \in N(p)} \min(v_{pq}, 0)(u_q^{n+1} - u_p^{n+1}). \tag{47}$$

The diffusion term (III) is approximated using a semi-implicit scheme

$$\text{(III)} \approx w_{\text{dif}} \, |\nabla u_p^n| \, g_p \sum_{q \in N(p)} \frac{m(e_{pq})}{m(\sigma_{pq})} \, \frac{u_q^{n+1} - u_p^{n+1}}{|\nabla u_{pq}^n|}. \tag{48}$$

Combining the terms (I), (II) and (III), we get the complete discretization of (38)

$$\frac{u_p^{n+1} - u_p^n}{\tau} m(p) + \sum_{q \in N(p)} \min(v_{pq}, 0)(u_q^{n+1} - u_p^{n+1}) = w_{\text{dif}} \, |\nabla u_p^n| \, g_p \sum_{q \in N(p)} \frac{m(e_{pq})}{m(\sigma_{pq})} \, \frac{u_q^{n+1} - u_p^{n+1}}{|\nabla u_{pq}^n|} \tag{49}$$

which is a linear system with unknowns u_p^{n+1}. We solve it using the Successive Over-Relaxation (SOR) method.

The Evans-Spruck regularization [31] is used to prevent division by zero due to zero gradients in the denominators

$$|\nabla u_{pq}^n| \approx |\nabla u_{pq}^n|_\varepsilon = \sqrt{\varepsilon^2 + |\nabla u_{pq}^n|^2}, \quad \varepsilon > 0. \tag{50}$$

We use the reduced diamond-cell approximation [31] to compute the norm of the gradient $|\nabla u_{pq}^n|_\varepsilon$ and $|\nabla I|_q$. The terms g_p and $|\nabla u_p^n|_\varepsilon$ are obtained using the mean value of $|\nabla I|_q$ and $|\nabla u_{pq}^n|$ in the neighbouring finite volume q

$$g_p = g\left(\frac{1}{6} \sum_{q \in N_p} |\nabla I|_q\right), \qquad |\nabla u_p^n|_\varepsilon = \sqrt{\frac{1}{6} \sum_{q \in N_p} |\nabla u_{pq}^n|^2 + \varepsilon^2}.$$

We define an approximation of the gradient of the edge detector g using central differences [33]

$$\nabla g_p = (G_{pe}, G_{pn}, G_{pt}) = (-G_{pw}, -G_{ps}, -G_{pb}),$$

where

$$G_{pe} = -G_{pw} \approx \frac{g_e - g_w}{2h_x}, \quad G_{pn} = -G_{ps} \approx \frac{g_n - g_s}{2h_y}, \quad G_{pt} = -G_{pb} \approx \frac{g_t - g_b}{2h_z}.$$

Another approach for approximating the gradient of the edge detector is suggested in [29, 31], which is particularly convenient for sharp edges. The current choice is convenient for images with weak or missing edges.

4.4. Results

In this section, we present the results of aortic segmentation using the GSUBSURF model for the entire dataset. Fig. 10 presents the segmentation result for patient 1, in 2D views. The slices are chosen from the abdominal and the thoracic aorta.

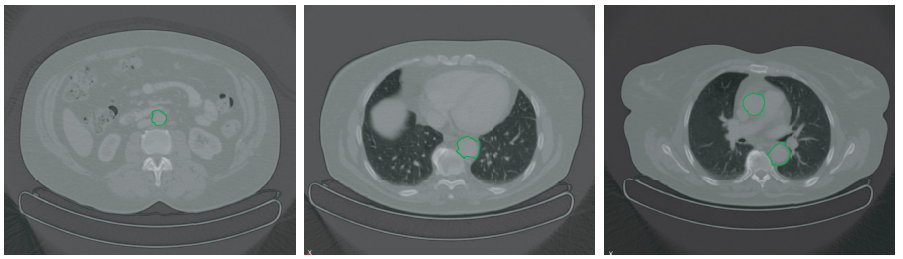

FIGURE 10. Segmentation result, 2D view (axial view) at three aorta regions in patient 1 image data.

Fig. 11 shows the results of the GSUBSURF segmentation in a 3D view for the datasets. The segmentation process is stopped when the L_2 norm between the previous and current solution is less than a given tolerance $\text{tol} = 0.001$. The grid size for each patient is taken equal to the voxel size (see Table 1). The edge detector parameter is $K = 100000$ for all patients,

$$\tau = 0.5, w_{\text{ad}} = 1.0, w_{\text{dif}} = 0.05 \quad \text{and} \quad \varepsilon = 0.001.$$

The choice of the isosurfaces for visualization (and later for accuracy estimation) is based on the histogram of the segmentation function. In fact, inside the segmented object, we have many voxels with similar high values, many voxels with similar low values outside the object, and few voxels in the transition layer. The largest gap in the histogram indicates the shock in the segmentation function, so we choose an isosurface in the gap [12].

We estimate the accuracy of our segmentation results using the Hausdorff distance [19]. Given two finite sets of points, $A = \{a_1, \ldots, a_m\}$ and $B = \{b_1, \ldots, b_l\}$, the mean Hausdorff distance is defined as

$$\text{MHD}(A, B) = \max\big(\text{mhd}(A, B), \text{mhd}(B, A)\big), \tag{51}$$

where

$$\text{mhd}(A, B) = \frac{1}{m} \sum_{i=1}^{m} \min_{b \in B} ||a_i - b|| \tag{52}$$

and $||\cdot||$ is the Euclidean distance between points of A and B. The set A consists of voxels (points) corresponding to the reference segmentation (manual segmentation) of the aorta, and B represents the set of voxels of the GSUBSURF segmentation results. We performed the manual segmentations using the software *3D Slicer*.

(A) P1, isosurface 0.2 (B) P2, isosurface 0.2 (C) P3, isosurface 0.3

(D) P4, isosurface 0.3 (E) P5, isosurface 0.17 (F) P6, isosurface 0.3

FIGURE 11. 3D rendering of the segmentation results for the data sets.

TABLE 3. Mean Hausdorff distance of segmentation results.

Patients	1	2	3	4	5	6
MHD	1.85	2.2	1.57	1.72	2.78	1.9

As shown in Table 3, the segmentation results overlap well with the reference segmentations. The maximum mean Hausdorff distance is 2.78 (patient 5), representing the worst-case scenario. That value corresponds to 3 voxels in x or y directions but less than 2 voxels in!z direction. These results suggest that our segmentation framework achieved high overlap with the reference segmentations,

indicating good performance. Nevertheless, as non-expert annotations generate the reference segmentation (manual), these results should be interpreted as indicative rather than definitive.

5. Application to the diagnosis of vasculitis

Large-vessel vasculitis (LVV) is the most common type of vasculitis affecting the aorta predominantly and has two major variants: Giant Cell Arteritis (GCA) and Takayasu Arteritis (TA) [15, 20, 40, 42]. TA usually affects people under 50, whereas GCA affects people over 50 [20]. Various approaches are used to diagnose LVV, including biopsy and FDG-PET/CT imaging. Imaging with FDG-PET/CT is a non-invasive approach used to visualize metabolic activity in the body and detect abnormalities. It can detect diseases in their early stage [4].

5.1. Diagnosis of LVV by FDG-PET/CT imaging

The literature review reveals that most studies on the diagnosis of LVV using FDG-PET/CT imaging have been conducted by experts in nuclear medicine, radiology, rheumatology, and vascular surgery. Therefore, our work is not to presume to replace them, but to offer a mathematical/software solution that can help them in their work. There is consensus on several questions, including recommended procedures for diagnosing LVV. For example, high FDG uptake in the aortic wall may help guide the diagnosis of LVV [5]. In clinical routine, an experienced nuclear medicine physician performs a visual analysis, which is considered positive when the FDG concentration, which we call uptake, in the region of interest (inflamed aortic regions) is higher than in the reference tissue (the liver) [4]. In the authors' recommendation papers [14,15], e.g., the assessment is based on visual analysis of the affected aortic region's uptake, and liver uptake is used as background when the vessel's visual analysis is "unclear". In another recommendation paper [40], the authors propose the use of a standardized 0–to–3 visual grading scale as follows:

- **0** = no uptake,
- **1** = low-grade uptake (vascular uptake $<$ liver uptake),
- **2** = intermediate-grade uptake (vascular uptake $\approx$ liver uptake),
- **3** = high-grade uptake (vascular uptake $>$ liver uptake),

where grade 2 is "possibly positive", and grade 3 is considered positive for active LVV. The authors of [40] emphasize that visual analysis is not always enough for an optimal assessment. Therefore, they discuss some (semi-) quantitative methods for further classification. The target-to-background ratio (TBR) approach utilises various structures, such as the lung, liver, or blood pool,

as a background. The SUV represents FDG uptake in the patient's organs, measured over a specified time interval after FDG administration, and normalized to the injected FDG dose and the patient's body weight [7]. Using the liver as the background is the most common approach for interpreting FDG-PET images [40]. In practice, ROIs are manually drawn around the target aorta regions, and parameters such as SUV_{max} and SUV_{mean} are computed within these ROIs. The authors of [26] recommend defining a spherical volume that encompasses the wall of the aorta in the aortic segment with the highest FDG uptake. For the background organ, a 3 cm diameter sphere is used to define the ROI in the right lobe of the liver to minimize the risk of including veins and arteries that run through the liver [40]. As the authors of [7] emphasize in their work, the parameters SUV_{max} and SUV_{mean} strongly depend on the definition of ROI. Therefore, there is a clear need to define the precise ROIs to ensure that the quantitative analysis is robust and reproducible. Several studies have previously addressed these issues. The authors of [18] presented a literature review of the proposed segmentation approaches. We can read there that the proposed methods include thresholding and region growing and are applied directly to PET image data. However, the work [18] was not specifically dedicated to vasculitis but rather to general PET interpretation, including cancer diagnosis. These works (methods) often suffer from poor contrast and recurrent noise in PET. Consequently, our approach, which involves segmenting ROIs on CT (offering better resolution than PET), followed by alignment with PET, yields significant improvements in ROIs definition.

5.2. Application

In this section, we present the application of aorta centerline extraction and segmentation to the interpretation of PET images. Patient data were obtained for patients suspected of vasculitis.

5.2.1. Definition of the regions of interest

One of our objectives in this work is to define precise ROIs in the liver and the aorta to assess vasculitis. To obtain the liver ROI, we segment the liver from the CT data (see [2]), then compute its centroid, and define a spherical volume with a diameter of 3 cm. For the aorta, unlike in [26], where the authors define ROIs in the most affected aorta region, we define multiple ROIs using the centered path points and the aorta segmentation. Each point of the centered path is assigned the distance from the aorta boundaries plus one PET voxel size (see Table 2) to ensure that a sphere centered at that point (voxel) encompasses the boundaries of the aorta. Therefore, for each point of the centered path, we define an aorta ROI where we compute the maximum SUV, i.e., SUV_{max}.

5.2.2. Results

In this section, we present the results of our quantitative analysis of FDG--PET/CT images to assess vasculitis. The CT and FDG-PET images are aligned (registered) to identify FDG-PET regions corresponding to the extracted ROIs from the CT image. In this work, we assume that the FDG-PET image voxel values correspond to the SUV in each voxel.

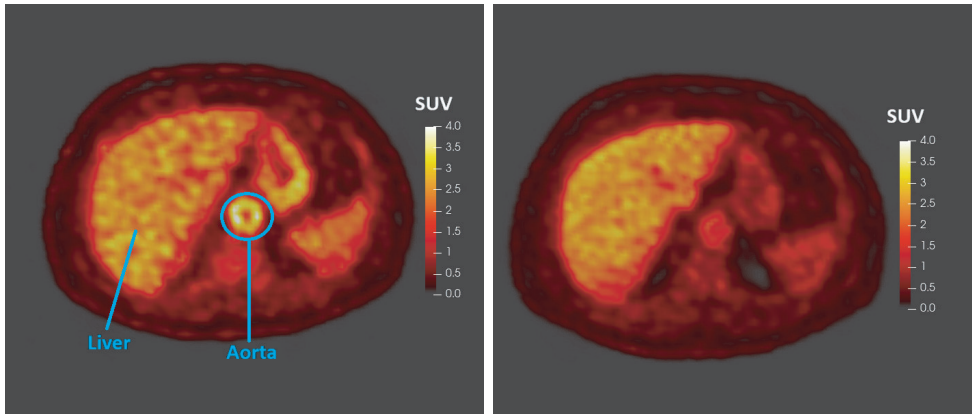

FIGURE 12. PET slice view of the aorta's highest SUV region before treatment (left) and the corresponding slice after treatment (right).

Fig. 12 shows the FDG uptake in the same plane for a patient before and after treatment. This slice was identified by analysing $\mathrm{SUV}_{\mathrm{ratio}}$

$$\mathrm{SUV}_{\mathrm{ratio}}(\mathrm{ROI}) = \frac{\mathrm{SUV}_{\mathrm{max}}^{\mathrm{aorta(ROI)}}}{\mathrm{SUV}_{\mathrm{mean}}^{\mathrm{liver(ROI)}}} \tag{53}$$

along the aorta, specifically selecting the slice with the maximal ratio to ensure optimal contrast. While pre-treatment analysis clearly suggests Grade 2 uptake, the post-treatment assessment (for the same slice) is more complex due to decreased metabolic activity within the vessel wall, not allowing for a straightforward visual interpretation. This example demonstrates that, as we suggest, automatic analysis can detect aortic regions with high FDG uptake and accurately define the grade (see Fig. 12 and the discussion in the next paragraph). This means that our framework can provide reproducible parameters ($\mathrm{SUV}_{\mathrm{ratios}}$) for diagnosing LVV from FDG-PET/CT image data.

In the following example, we present FDG-PET image interpretation based on the SUV ratios computed along the aorta.

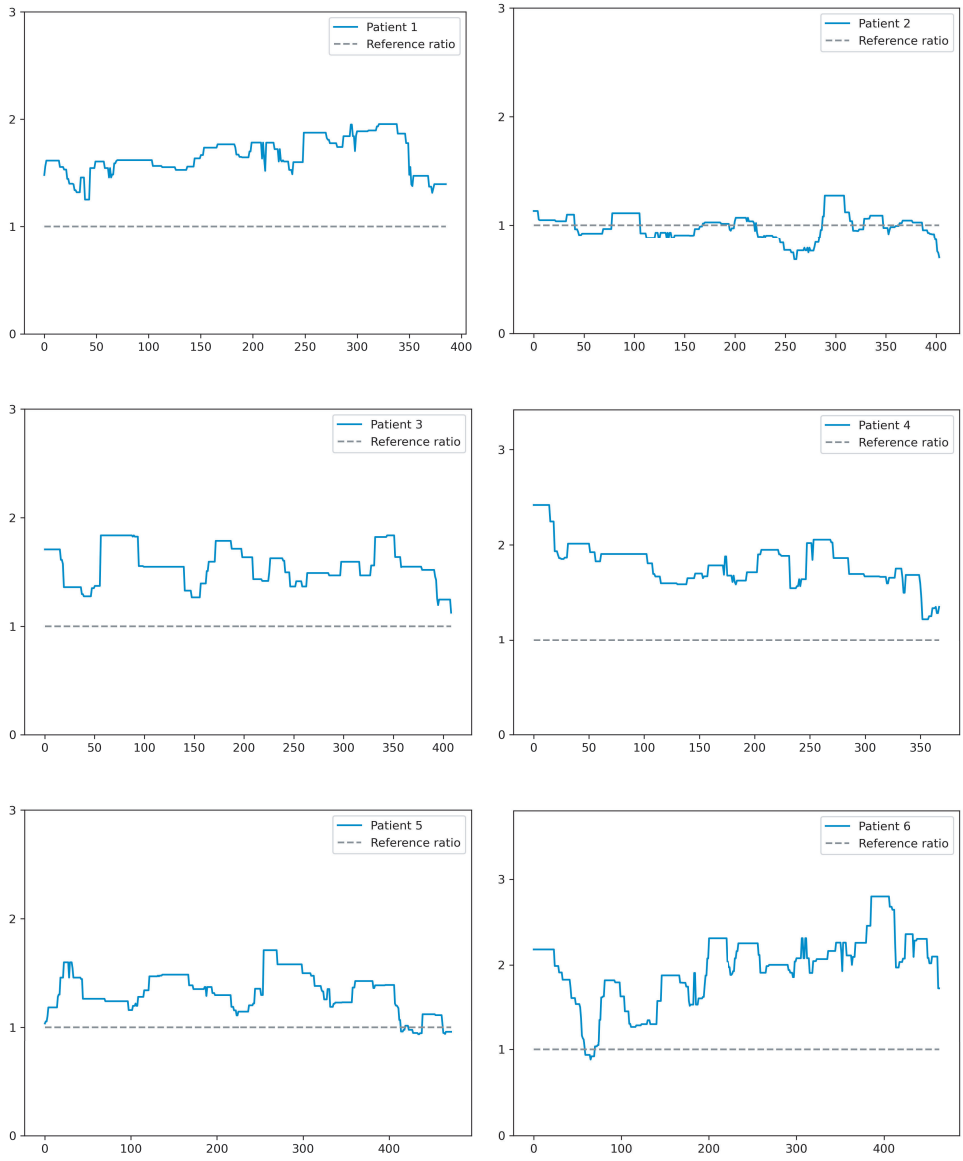

FIGURE 13. Ratio vascular uptake and liver uptake along the centered path for the dataset.

Fig. 13 presents the calculated ratios along the aorta for our dataset. The x-axis corresponds to the number of points along each aorta centerline. The y-axis corresponds to the calculated ratios (53). The gray line (dashed) corresponds to a ratio equal to 1. The graphs for patients 1, 3, and 4 indicate that vascular uptake significantly exceeds liver uptake along the aorta. This result suggests that the inflammation is extensive and a treatment is required. The graphs for patients 5 and 6 indicate that inflammation is localized to specific regions of the aorta. Since we have the aorta centerline, we can precisely identify these regions using the coordinates of the path points. The graph for patient 1 shows that aortic uptake exceeds liver uptake along the aorta. In contrast, the graph for patient 2 shows lower ratios than for patient 1, and some regions with higher liver uptake. Since these two images were obtained from the same patient, before and after treatment, we can conclude that the treatment has a positive effect on aortic inflammation. Visual analysis was not straightforward to assess whether vascular uptake was higher than the liver uptake in the right image of Fig. 12. However, with our proposed quantitative approach, we conclude that for that slice, liver uptake is larger. This example demonstrates that quantitative analysis can aid practitioners in their assessment when visual analysis alone is not sufficient to reach a conclusion.

6. Conclusion

In this paper, we propose a framework for segmenting the aorta from non-enhanced CT data. The segmented aorta is used to define the precise ROIs for the diagnosis of aortic vessel vasculitis using FDG-PET/CT image data. Our three--step approach is robust enough to handle the anatomical variability of the aortic shape. We proposed a new potential function to extract a path within the aorta using the minimal path approach with keypoints detection, given two endpoints. We utilize a 3D curve evolution model to align the initial path with the centerline of the aorta. The original work [33] computes the velocity vector field from the available segmentation. However, we do not have the segmented aorta as input. Therefore, we use edge detection and thresholding to extract the aorta's edges and construct the velocity vector field. This application demonstrates that the model proposed in [33] is robust enough to perform well even when some edges are missing. In the final step, we apply the GSUBSURF method, using the aorta's centerline as an initial condition to extract the aortic surface. Our proposed framework can process FDG-PET/CT image data with minimal user interaction. The framework can assist in assessing vasculitis when the visual analysis is inconclusive. Our future work will focus on automatically detecting endpoints for minimal path extraction, aiming to make the framework fully automatic.

Acknowledgments. The authors thank TatraMed Software s.r.o. for technical support and INFLANET for funding. This project has received funding from the European Union's Horizon 2020 research and innovation programme under the Marie Skłodowska-Curie grant agreement No. 955576.

REFERENCES

[1] ADAMS, R.—BISCHOF, L.: *Seeded region growing*, IEEE Transactions On Pattern Analysis and Machine Intelligence, **16** (1994), no. 6, 641–647.

[2] ALLALY, K. A.—URBÁN, J.: *Automatic path extraction inside the aorta from CT data*. In: Proceedings of the Conference Algoritmy (2024), pp. 255–263,

[3] AMBROZ, M.—BALAŽOVJECH, M.—MEDĽA, M.—MIKULA, K.: *Numerical modeling of wildland surface fire propagation by evolving surface curves*, Adv. Comput. Math. **45** (2009), 1067–1103.

[4] ARNAUD, L.—HAROCHE, J.—MALEK, Z.—ARCHAMBAUD, F.—GAMBOTTI, L.—GRIMON, G.—KAS, A.—COSTEDOAT-CHALUMEAU, N.—CACOUB, P.—TOLEDANO, D.—CLUZEL, P.—PIETTE, J.-C.—AMOURA, Z.: *Is ^{18}F-fluorodeoxyglucose positron emission tomography scanning a reliable way to assess disease activity in Takayasu arteritis?*, Arthritis & Rheumatism **60** (April 2009), 1193–1200.

[5] BALINK, H.—BENNINK, R. J.—VAN ECK-SMIT, B. L. F.—VERBERNE, H. J.: *The Role of ^{18}F-FDG PET/CT in large-vessel vasculitis: appropriateness of current classification criteria?*, BioMed Research International **2014** (2014), no. 1, 13 p. https://doi.org/10.1155/2014/687608

[6] BENMANSOUR, F.—COHEN, L. D.: *Fast object segmentation by growing minimal paths from a single point on 2D or 3D images*, J. Math. Imaging Vision **33** (2009), 209–221.

[7] BOELLAARD, R.—O'DOHERTY, M. J.—WEBER, W. A.—MOTTAGHY, F. M.—LONSDALE, M. N.—STROOBANTS, S. G.—OYEN, W. J. G.—KOTZERKE, J.—HOEKSTRA, O. S.—PRUIM, J. et al.: *FDG PET and PET/CT: EANM procedure guidelines for tumour PET imaging: version 1.0*, Eur. J. Nucl. Med. Mol. Imaging **37** (2010), no. 1, 181–200. DOI: 10.1007/s00259-009-1297-4.

[8] BANKMAN, I. N.: *Handbook of medical imaging: processing and analysis*. Academic Press, 2000.

[9] CASELLES, V.—KIMMEL, R.—SAPIRO, G.—SBERT, C.: *Minimal surfaces: a geometric three-dimensional segmentation approach*, Num. Math. **77** (1997), 423–451.

[10] CHEN, D.—COHEN, L. D.—MIREBEAU, J-M.: *Vessel extraction using anisotropic minimal paths and path score*, IEEE International Conference on Image Processing (ICIP), (2014), 1570–1574.

[11] COHEN, L. D.—KIMMEL, R.: *Global minimum for active contour models: a minimal path approach*, International Journal of Computer Vision **24** 1997, 57–78.

[12] CORSARO, S.—MIKULA, K.—SARTI, A.—SGALLARI, F.: *Semiiplicit covolume method in 3D image segmentation*, SIAM J. Sci. Comput. **28** (2006), 2248–2265.

[13] CASTELLANOS, M. D. C. P.—VEGA, M. M.—CABALLERO, A. M.— GONZÁLVEZ, M. P. B.: *Early diagnosis of large vessel vasculitis: usefulness of positron emission tomography with computed tomography*, Reumatología Clínica **9** (2013), 65–68.

[14] DEJACO, C.—RAMIRO, S.—BOND, M.—BOSCH, P.—PONTE, C.—MACKIE, S. L.—BLEY, T. A.—BLOCKMANS, D.—BROLIN, S.—BOLEK, E. C. et al.: *EULAR recommendations for the use of imaging in large vessel vasculitis in clinical practice: 2023 update*, Annals of the Rheumatic Diseases **83** (2024), 741–751.

[15] DEJACO, C.—RAMIRO, S.—DUFTNER, C.—BESSON, F. L.—BLEY, T. A.—BLOCKMANS, D.—BROUWER, E.—CIMMINO, M. A.—CLARK, E.—DASGUPTA, B.: *EULAR recommendations for the use of imaging in large vessel vasculitis in clinical practice*, Annals of the Rheumatic Diseases **77** (2018), 636–643.

[16] DESCHAMPS, T.—COHEN, L. D.: *Fast extraction of minimal paths in 3D images and applications to virtual endoscopy*, Medical Image Analysis **5** (2001), 281–299.

[17] GAMECHI, Z. S.—BONS, L. R.—GIORDANO, M.—BOS, D.—BUDDE,R. P. J.—KOFOED, K. F.—PEDERSEN, J. H.—ROOS-HESSELINK, J. W.—DE BRUIJNE, M.: *Automated 3D segmentation and diameter measurement of the thoracic aorta on non-contrast enhanced CT*. European Radiology **29** (2019), 4613–4623.

[18] HATT, M.—LAMARE, L.—BOUSSION, N.—TURZO, A.—COLLET, C.—SALZENSTEIN, F.—ROUX, C.—JARRITT, P.—CARSON, K.—CHEZE-LE-REST, C.—VISVIKIS, D.: *Fuzzy hidden Markov chains segmentation for volume determination and quantitation in PET*, Physics in Medicine and Biology **52** (2007), 3467–3491.

[19] HUTTENLOCHER, D. P.—KLANDERMAN, G. A.—RUCKLIDGE, W. J.: *Comparing images using the Hausdorff distance*, IEEE Transactions on Pattern Analysis and Machine Intelligence **15** (1993).

[20] JENNETTE, J. C.—FALK, R. J.—BACON, P. A.—BASU, N.—CID, M. C.—FERRARIO, F.—FLORES-SUAREZ, L. F.—GROSS, W. L.—GUILLEVIN, L.—HANGEN, E. C. et al.: *2012 revised international chapel hill consensus conference nomenclature of vasculitides*, Arthritis and Rheumatism **65** (January 2013), 1–11.

[21] KASS, M.— WITKINS, A.—TERZOPOULOS, D.: *Snakes: active contours model*, International Journal of Computer Vision (1988), pp. 321–331. https://doi.org/10.1007/bf00133570

[22] KOVÁCS, T.: *Automatic Segmentation of the Vessel Lumen from 3D CTA Images of Aortic Dissection*. PhD thesis, ETH Zurich, 2010.

[23] KRIVÁ, Z.—MIKULA, K.—PEYRIÉRA, N.—RIZZI, B.—SARTI, A.— STAŠOVÁ, O.: *3D early embryogenesis image filtering by nonlinear partial differential equations*, Medical Image Analysis **14** (2010), 510–526.

[24] KURUGOL, S.—ESTEPAR, R. S. J.— ROSS, J.—WASHKO, G. R.: *Aorta segmentation with a 3D level set approach and quantification of aortic calcifications in non-contrast chest CT*, Conference Proceedings IEEE Eng. Med. Biol. Soc. **16** (2012), 2343–2346.

[25] LI, H.—YEZZI, A.: *Vessels as 4D curves: global minimal 4D paths to extract 3D tubular surfaces and centerlines*, IEEE Transactions on Medical Imaging **26**, (September 2007).

[26] LMFELD, S.—ROTTENGURGER, C.—SCHEGK, E.—ASCHWANDEN, M.—JUENGLING, F.—STAUB, D.—RECHER, M.—KYNURZ, D.—BERGER, C. T.—DAIKELER. T.: *[^{18}F]FDG positron emission tomography in patients presenting with suspicion of giant cell arteritis - lessons from a vasculitis clinic*, European Heart Journal - Cardiovascular Imaging **19** (August 2018), 933–940.

[27] MARTÍNEZ-MERA, J. A.—TAHOCES, P. G.—CARREIRA, J. M.—SUÁREZ-CUENCA, J. J.—SOUTO. M.: *A hybrid method based on level set and 3D region growing for segmentation of the thoracic aorta*, Computer Aided Surgery **18** (2013), 109–117.

[28] MIKULA, K.—OHLBERGER, M.—URBÁN. J.: *Inflow-implicit/outflow-explicit finite volume methods for solving advection equations*, Appl. Numer. Math. **85** (June 2014), 16–37.

[29] MIKULA, K.—PEYRIÉRAS, N.—REMIŠÍKOVÁ, M.—SARTI, A.: *3D embryogenesis image segmentation by the generalized subjective surface method using the finite volume technique*. Finite Volumes for Complex Applications V: Problems and Perspectives (2008), 585–592.

[30] MIKULA, K.—PEYRIÉRAS, N.—REMIŠÍKOVÁ, M.—STAŠOVÁ, O.: *Segmentation of 3D cell membrane images by PDE methods and its applications*, Computers in Biology and Medicine **41** (2011), 326–339.

[31] MIKULA, K.—REMEŠÍKOVÁ, M.: *Finite volume schemes for the generalized subjective surface equation in image segmentation*, Kybernetika, **45** (2009), 646–656.

[32] MIKULA, K.—SMISEK, M.—SIPR, R.: *Parallel algorithms for segmentation of cellular structures in 2d+time and 3d morphogenesis data*. In Proceedings of ALGORITMY **2012** (2015), pp. 416–426; `https://www.math.sk/mikula/43Smisek.pdf`

[33] MIKULA, K.—URBÁN, J.: *A new tangentially stabilized 3D curve evolution algorithm and its application in virtual colonoscopy*, Adv. Comput. Math. **40** (August 2014), 819–837.

[34] MIKULA, K.—ŠEVČOVIČ, D.: *Evolution of plane curves driven by a nonlinear function of curvature and anisotropy*, SIAM J. Appl. Math. **61** (2001), 1473–1501.

[35] MIKULA, K.—ŠEVČOVIČ, D.: *A direct method for solving an anisotropic mean curvature flow of planar curve with an external force*, Mathematical Methods in Appl. Sci. **27** (2004), 1545–1565.

[36] MIREBEAU, J.-M.: *Anisotropic fast-marching on cartesian grids using lattice basis reduction*, SIAM J. Numer. Anal. (Society for Industrial and Applied Mathematics (SIAM)) **52** (2014), 1573–1599.

[37] PERONA, P.—MALIK. J.: *Scale-space and edge detection using anisotropic diffusion*, IEEE Transactions on Pattern Analysis and Machine Intelligence, **12** (July 1990), 629–639.

[38] SARTI, A.—CITTI. G.: *Subjective surfaces and Riemannian mean curvature flow of graphs*. In: Proceedings of Algoritmy **2000** (2001), no. 1, pp. 85–103.

[39] SETHIAN, J. A.: *A fast marching level set method for monotonically advancing fronts*. In: Proceedings of the Natural Academy of Sciences **93** (February 1996), pp. 1591–1595.

[40] SLART, R. H. J.—GLAUDEMANS, A. W. J. M.—CHAREONTHAITAWEE, P.—TREGLIA, G.—BESSON, F. L.—BLEY, T. A.—BLOCKMANS, D.—BOELLARD, R.—BUCERIUS, J.— CARRIL, J. M. et al.: *FDG-PET/CT(A) imaging in large vessel vasculitis and polymyalgia rheumatica: joint procedural recommendation of the EANM, SNMMI, and the PET interest group (PIG), and endorsed by the ASNC*, European Journal of Nuclear Medicine and Molecular Imaging **45** (2018), 1250–1269.

[41] TRULLO, R.—PETITJEAN, C.—RUAN, S.—DUBRAY, B.—NIE, D.—SHEN. D.: *Segmentation of organs at risk in thoracic CT images using a sharpmask architecture and conditional random fields*. In: 2017 IEEE 14th international symposium on biomedical imaging IEEE **2017** (2017), pp. 1003–1006.

[42] ŠTEŇOVÁ, E.—MIŠTEC, S.— POVINEC. P.: *FDG-PET/CT in large-vessel vasculitis: its diagnostic and follow-up role*, Rheumatology International **30** (August 2009), 1111–1114.

[43] XIE, Y.—PADGETT, J.—BIANCARDI, A. M.—REEVES, A. P.: *Automated aorta segmentation in low-dose chest CT images*, International Journal of Computer Assisted Radiology and Surgery **9** (2014), 211–219.

[44] YUAN, J.—PEPE, A.—LI, J.—GSAXNER, C.—ZHAO, F.-H.—POMYKALAD, K. L.—KLEESIEK, J.—FRNAGI, A. F.—EGGER, J.: *AI-based aortic vessel tree segmentation for cardiovascular diseases treatment: status quo*, arXiv preprint arXiv, 2021.

[45] ZHAO. H.: *A fast sweeping method for eikonal equations*, Mathematics of Computation **74** (2004), 603–627.

Received November 12, 2025
Revised March 3, 2026
Accepted March 15, 2026
Publ. online April 30, 2026

Konan A. Allaly
Karol Mikula
Department of Mathematics and Descriptive Geometry
Faculty of Civil Engineering
Slovak University of Technology
Radlinskeho 11,
81005 Bratislava
SLOVAKIA

E-mail: allaly.anderson@stuba.sk
karol.mikula@stuba.sk

Konan A. Allaly
Jozef Urbán
TatraMed Software s.r.o.
Líščie údolie 9
84104 Bratislava
SLOVAKIA

E-mail: konan.allaly@tatramed.sk
jozef.urban@tatramed.sk